3
Mathematical modeling of the torsional dynamics of a drill string

3.1
Introduction

Many works about torsional vibrations on drilling systems [1, 12, 18, 24, 41] have been published using different numerical models. The model choice depends on the objectives of the work. Deterministic models have been largely applied. However stochastic models have gained ground on the academic drilling researches in order to provide a best description the drilling conditions in the borehole and estimation of final costs [31]. Nevertheless, these stochastic models presents a high computational cost making it difficult to apply in real time. In this dissertation, a deterministic model is presented aiming to achieve fast computational performance, identifying torsional vibration maps and find a best way to mitigate torsional vibrations. The definition of torsional vibration map is presented in the next section.

First, the dynamic model by means a lumped parameters approach of the oil well drilling system is described in section 3.2. Also in this chapter, there are friction torque models to characterize the resistive torque on bit. A criterion for acceptable torsional vibrations is established in order to distinguish the zones of acceptable and unacceptable torsional vibrations. Comparisons between the torsional vibration maps from the different friction models are performed (section 3.3).

In order to identify the proper discretization of the drill string, a convergence analysis is performed in section 3.4. Discretization criteria is defined by observing the second and third natural frequencies of the system. Relative errors are analyzed to justify the chosen number of degrees of freedom.

The numerical results of the full models are discussed in section 3.5. Bifurcation diagrams, limit cycles, and nonlinear jumps are illustraded in order to observe the nonlinear behavior of the drill string system under differents sets of weight on bit and surface RPM. The stability of the solutions observed are discussed in this section.

Finally, section 3.6 ends summarizing the conclusions of the discussed content in this chapter. All the state-space models of the torsional dynamics of the drilling that will be shown are solved using *MatLab* solvers such as *ODE23t* (for moderately stiff equation systems). In Appendix A is presented a brief explanation about the method adopted for this solver.

3.2 Torsional model

3.2.1 First modeling approach: two degrees of freedom

First, the dynamic model consists of two DOF where the Surface Torque (STOR) is imposed at the top end (see Figure 3.1), as a torsional double pendulum. The first researcher to approach the drilling system as a torsional pendulum was Jansen in several works [17, 18, 16] The electrical equations of the top drive motor are not implemented, and the axial and lateral dynamics of the drilling system are neglected. The BHA is assumed to be a rigid body since its stiffness is much greater than the drill pipe stiffness k, reaching two orders of magnitude as seen in Eq. 3-1 below,

$$\frac{k}{K_{BHA}} = 0.008. \tag{3-1}$$

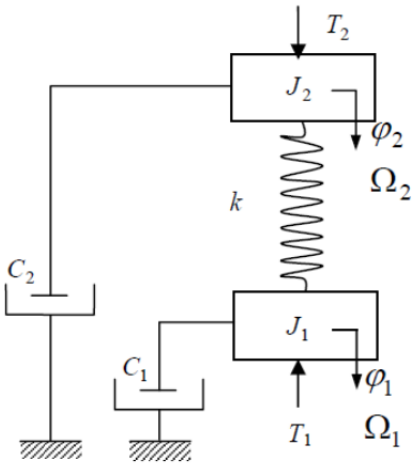

Figure 3.1: Torsional model of two degrees of freedom.

The two DOF modeling is governed by Eq. 3-2, as follows.

$$\begin{bmatrix} J_1 & 0 \\ 0 & J_2 \end{bmatrix} \begin{bmatrix} \dot{\Omega}_1 \\ \dot{\Omega}_2 \end{bmatrix} + \begin{bmatrix} C_1 + C_s & -C_s \\ -C_s & C_2 + C_s \end{bmatrix} \begin{bmatrix} \Omega_1 \\ \Omega_2 \end{bmatrix} + \begin{bmatrix} k & -k \\ -k & k \end{bmatrix} \begin{bmatrix} \varphi_1 \\ \varphi_2 \end{bmatrix} = \begin{bmatrix} -T_1 \\ T_2 \end{bmatrix} \tag{3-2}$$

where T_1 is the Torque on Bit, T_2 is the surface torque. J_1 and J_2 the equivalent moment of inertia at bottom end and top end, respectively. C_1 and C_2 are the mud damping, Ω_1 the bit speed and Ω_2 the top drive speed (Surface RPM - SRPM), C_s the structural damping, φ_1 and φ_2 the rotational displacement (angle) of the bit and top drive, respectively, starting with zero at time $t = 0$, and k is the equivalent stiffness of the drill pipe.

Defining the lengths L_{DP}, L_{BHA}, the densities ρ_{DP}, ρ_{BHA} (kg/m^3), the outer diameters OD_{DP}, OD_{BHA}, the inner diameters ID_{DP}, ID_{BHA}, the area moments of inertia I_{DP}, I_{BHA} for the drill pipe, and the bottom hole assembly, respectively. The area moments of inertia are given by

$$I_{BHA} = \frac{\pi}{32}\left(OD_{BHA}^4 - ID_{BHA}^4\right), \tag{3-3a}$$

$$I_{DP} = \frac{\pi}{32}\left(OD_{DP}^4 - ID_{DP}^4\right). \tag{3-3b}$$

From Eq. 3-3b, the stiffness k is given by

$$k = \frac{G\, I_{DP}}{L_{DP}}, \tag{3-4}$$

where G is the shear modulus $G = \frac{E}{2(1+\nu)}$.

The equivalent mass moment of inertia of the BHA may be written

$$J_1 = \rho_{BHA}\, I_{BHA}\, L_{BHA}, \tag{3-5}$$

and the mass moment of inertia in top end is assumed 1000 $kg\, m^2$.

The mud damping is written in terms of a damping factor of the mud Dr,

$$C_1 = Dr\ L_{DP}. \tag{3-6}$$

The structural damping is given by $C_s = 2\,\xi\,\sqrt{k\, J_1}$, where ξ is the damping factor. The damping factor value is $\xi = 0.02$.

3.2.2 Second modeling approach: multiple degrees of freedom

Afterwards, the analysis is made including more than two DOF's and then modeled as illustrated in Figure 3.2. The J_{BHA} is obtained as 3-5 and the mass moment of inertia of the drill pipes is given by Eq. 3-7, as follows

$$J_p = \rho_{DP}\, I_{DP}\, L_{DP}. \tag{3-7}$$

In this multiple degrees of freedom modeling, the matrix of inertia $\underline{\mathbf{J}}$, damping

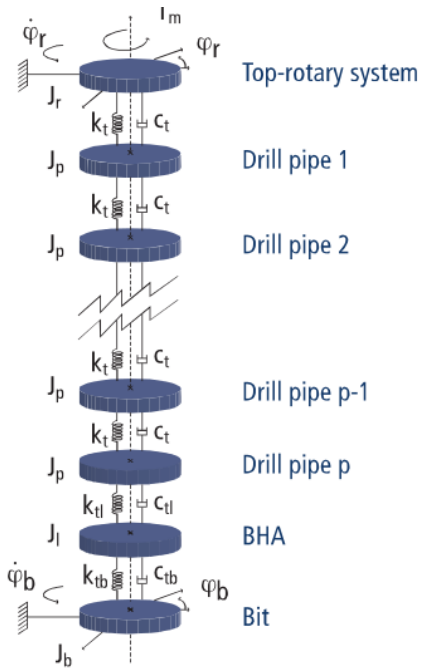

Figure 3.2: Torsional model of multiple degrees of freedom. Source: López [27].

$\underline{\mathbf{C}}$ and stiffness $\underline{\mathbf{K}}$ are expressed in Eqs. 3-8, as follows

$$\underline{\mathbf{J}} = \begin{bmatrix} J_1 & 0 & \cdots & \cdots & 0 \\ 0 & \ddots & 0 & \cdots & \vdots \\ \vdots & 0 & \ddots & 0 & \vdots \\ \vdots & \cdots & 0 & \ddots & 0 \\ 0 & \cdots & \cdots & 0 & J_n \end{bmatrix},$$

$$\underline{\mathbf{C}} = \begin{bmatrix} C_1 + C_{s_1} & -C_{s_1} & 0 & \cdots & \cdots & 0 \\ -C_{s_1} & C_2 + C_{s_1} + C_{s_2} & -C_{s_2} & 0 & \cdots & \vdots \\ 0 & -C_{s_2} & \ddots & -C_{s_3} & 0 & \vdots \\ \vdots & 0 & \ddots & \ddots & \ddots & 0 \\ \vdots & \cdots & 0 & -C_{s_{n-2}} & \ddots & -C_{s_{n-1}} \\ 0 & \cdots & \cdots & 0 & -C_{s_{n-1}} & C_{s_n} + C_{s_{n-1}} \end{bmatrix}$$

$$,\underline{\mathbf{K}} = \begin{bmatrix} k_1 & -k_1 & 0 & \cdots & \cdots & 0 \\ -k_1 & k_1 + k_2 & -k_2 & 0 & \cdots & \vdots \\ 0 & -k_2 & \ddots & -k_3 & 0 & \vdots \\ \vdots & 0 & \ddots & \ddots & \ddots & 0 \\ \vdots & \cdots & 0 & -k_{n-2} & \ddots & -k_{n-1} \\ 0 & \cdots & \cdots & 0 & -k_{n-1} & -k_{n-1} \end{bmatrix},$$

where n represents the number of degree of freedom in these equations and the

matrices will be underlined. In multi degree of freedom, the structural damping is calculated as $C_{s_i} = 2\,\xi\,\sqrt{k_i\,J_i}$. The viscous damping from the mud is similarly calculated by Eq. 3-6, assuming the form $C_i = Dr\;L_{DP_i}$, where i identifies the DOF.

For solving a second order differential equation, the initial conditions of motion are necessary. Herein, φ_0 and Ω_0 denote initial conditions vectors of angular displacements and velocities, respectively, of the degrees of freedom, as Eqs. 3-9 below

$$\varphi_0 = [\varphi_{1_0}\;\varphi_{2_0}\;...\,\varphi_{n_0}]^T, \tag{3-9a}$$

$$\Omega_0 = [\Omega_{1_0}\;\Omega_{2_0}\;...\,\Omega_{n_0}]^T. \tag{3-9b}$$

where the superscript T denotes transposition. For convenience, the equations of motions are written as state-space (Eq. 3-10).

$$\mathbf{q}' = \underline{\mathbf{A}}\,\mathbf{q} + \mathbf{T}, \tag{3-10}$$

where $\underline{\mathbf{A}}$ is the matrix ($2n$ x $2n$) that contains the proprieties of the system, $\mathbf{T}$ is the vector ($2n$ x 1) with external torques and $\mathbf{q}$ is the state-space coordinate vector ($2n$ x 1). Eqs. 3-11 describes each member of Eq. 3-10, as follows

$$\mathbf{q} = \begin{bmatrix} \varphi_1 \\ \vdots \\ \varphi_n \\ \Omega_1 \\ \vdots \\ \Omega_n \end{bmatrix}, \underline{\mathbf{A}} = \begin{bmatrix} \underline{\mathbf{0}} & \underline{\mathbf{I}} \\ \underline{\mathbf{J}}^{-1}(-\underline{\mathbf{K}}) & \underline{\mathbf{J}}^{-1}(-\underline{\mathbf{C}}) \end{bmatrix}, \mathbf{T} = \underline{\mathbf{J}}^{-1} \begin{bmatrix} 0 \\ \vdots \\ 0 \\ -T_1 \\ 0 \\ \vdots \\ 0 \\ T_n \end{bmatrix}. \tag{3-11}$$

The $\underline{\mathbf{I}}$ denotes the identity matrix (n x n) and $\underline{\mathbf{0}}$ denotes the zeros matrix (n x n). The parameters used in the simulations are described in Table 3.1.

3.2.3 Severity criteria

The severity criteria is given by Eq. 3-12. This equation is used in industry to evaluate the stick-slip severity (SSS). For example, if the SSS is equal to 1 it means that the oscillation amplitude reaches the double value of the SRPM. In Figure 3.3 is shown the two degrees of freedom system in torsional vibrations and the limit line which separates vibration and no vibration zones. The weight on bit (WOB) is applied after 60 seconds to eliminate the transient behavior of the drilling system.

Parameter	Description	Value	Unit
ρ_{dp}	Drill string mass density	7850	kg/m^3
L_{dp}	Drill string length	2780	m
OD_{dp}	Drill string outer diameter	0.1397	m
ID_{dp}	Drill string inner diameter	0.1186	m
ρ_{bha}	BHA mass density	7850	kg/m^3
L_{bha}	BHA length	400	m
OD_{bha}	BHA outer diameter	0.2095	m
ID_{bha}	BHA inner diameter	0.0714	m
E	Young's modulus	210	GPa
ν	Poisson ratio	0.33	–

Table 3.1: Numerical values of the drill string system.

$$SSS = \left(\frac{DRPM_{max} - DRPM_{min}}{2\,SRPM}\right) \cdot 100. \tag{3-12}$$

The maximum and minimum bit speed are $DRPM_{max}$ and $DRPM_{min}$, respectively. $SRPM$ is the imposed speed at surface. It means the calculation of the oscillation amplitude was compared to the imposed speed at surface. The value SSS is compared with an empirical value 15 %, i.e., if SSS is greater or equal to 15 % the system will be on undesirable torsional vibration otherwise the system will not be on undesirable torsional vibration.

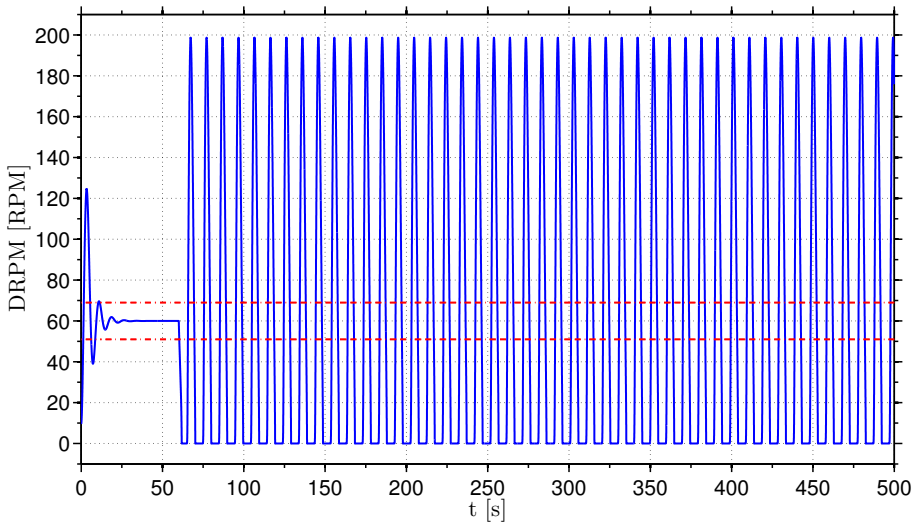

Figure 3.3: Downhole speed under torsional vibrations and the limit line (dashed red line) for a set of 60 RPM and 110 kN.

3.3 Sensitivity analysis of the friction torque models

The torque applied at the bottom end is modeled as a friction responsible to dissipate energy of the system. Several works, such as reference [21, 29], have been model this friction torque on bit as shown in Eq. 3-13, where P_f is the proportional factor (it may be related with the radius of the bit), WOB is the weight on bit and $\mu(\Omega_1)$ represents the friction coefficient as function of the angular velocity at the bottom end. In Table 3.2 the points used to create the friction models from the "look-up table" function (*Simulink*) are shown. This procedure eliminates numerical problems from the friction models adopted since it performs a linear interpolation between these points (see Figure 3.4).This is the function to obtain the friction coefficient $\mu(\Omega_1)$. For the simulations, the friction resistive torque is applied after 60 seconds. These, and other, friction models are detailed in references [23, 14].

Some approaches (considering axial motion or not) as in [21], the weight on bit may be not constant. Herein, the WOB and the P_f are considered constants. Importantly, the analysis performed here intends to observe the dynamics of the drill string under different friction torques and does not to model the friction torque acting on bit. Therefore approximated friction torque models are proposed.

In order to understand the torsional behavior of the drilling system, a sensitivity analysis on the friction torque model at the bit is performed. First, four friction torque models (see Figure 3.5) are applied to generate charts of the torsional vibration map.

The torsional vibration map represents a map of set-points WOB x RPM. This is because these parameters are the main control parameters in field operations, i.e. the driller provides a input of weight on bit and surface RPM of the drilling system and may change this parameters when it is necessary. The curve divides this map in two zones: with or without undesirable torsional vibrations.

$$T_1(\Omega_1) = P_f \cdot WOB \cdot \mu(\Omega_1), \tag{3-13}$$

The models illustrated in Figure 3.5 are three Modified Coulomb Frictions (MCF), and Decay friction. These Modified Coulomb Frictions present a difference between static and dynamic points. Also, the difference between the MCF's is based on the value of the dynamic point. In Figure 3.6 is shown the static and dynamic friction points on a friction chart. For all of the friction models, the static friction and the dynamic friction remain the same: 1.1 and 1, respectively.

Figure 3.7 shows the torsional vibration map with the friction models described above. Also, it presents a red and black points to illustrate the torsional behavior in these zones, using the Model 2, as it shown in Figure 3.8. It is worth mentioning that the system response to three MCF's are similar, meaning that slight changes on the dynamic point do not modify significantly the torsional vibration map. Model 6 (Decay model) shows a behavior completely different from the others on the torsional vibration map.

Models	Description	Static Point [rad/s]	Dyn. Point [rad/s]
Model 1	MCF 1	0.001	0.0013
Model 2	MCF 2	0.001	0.05
Model 3	MCF 3	0.001	0.21
Model 4	Decay Friction	0.001	0.31

Table 3.2: Friction model parameters.

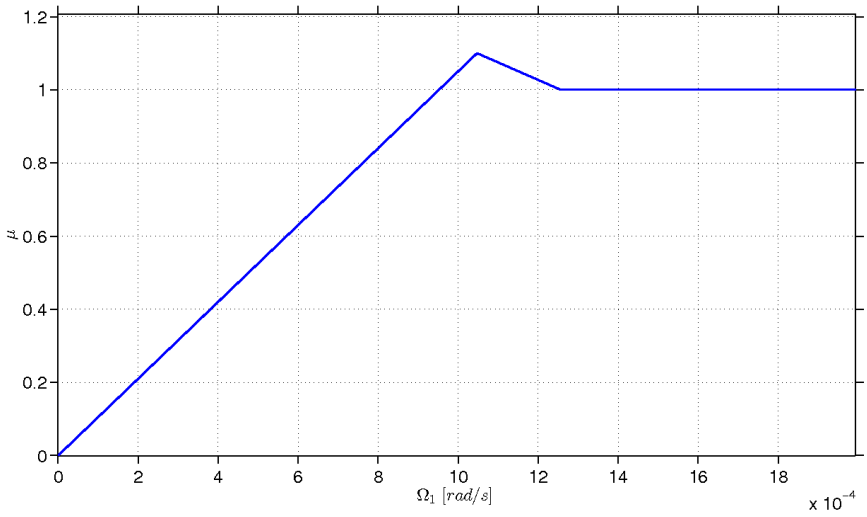

Figure 3.4: Linear interpolation to create the friction models adopted.

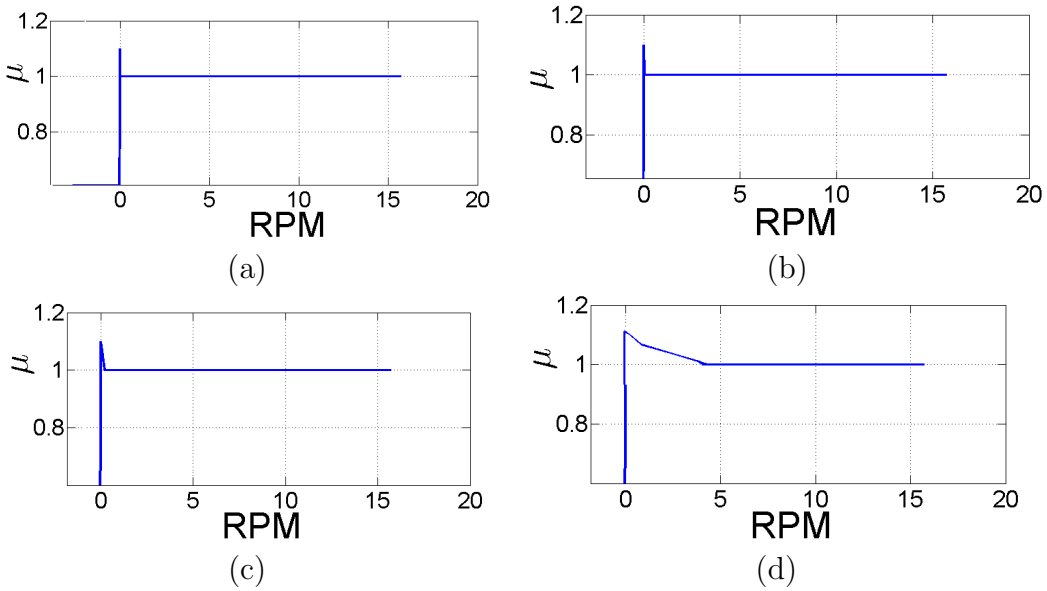

Figure 3.5: Applied friction models. (a) Model 1, (b) Model 2, (c) Model 3, and (d) Model 4.

Herein, a new concept is introduced to quantify the results: net area. Net area is the operation window without stick-slip, i.e., the area below the torsional vibration map. Thus, Model 6 presented a reduction of net area of approximately 32.5 % when compared with Models 1, 2, and 3.

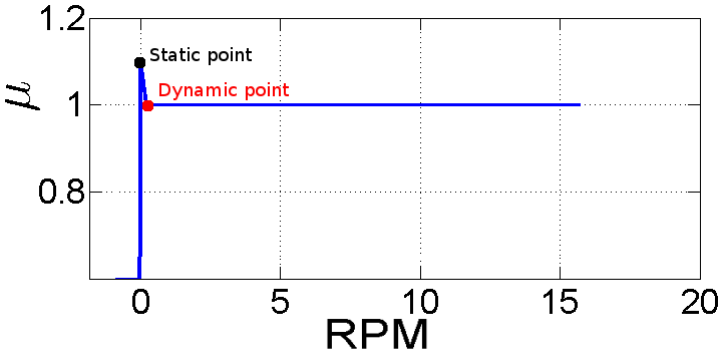

Figure 3.6: Static and dynamic points.

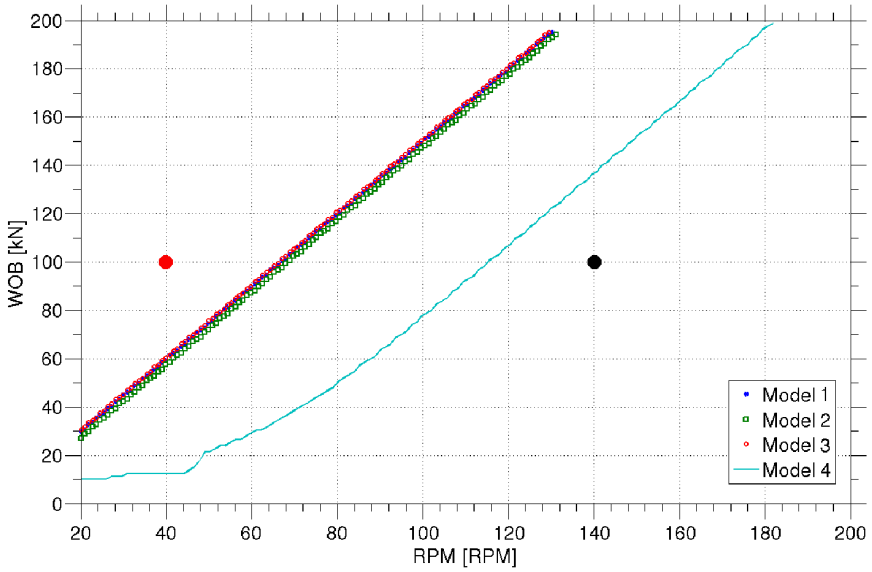

Figure 3.7: Torsional vibration map for the different friction torques.

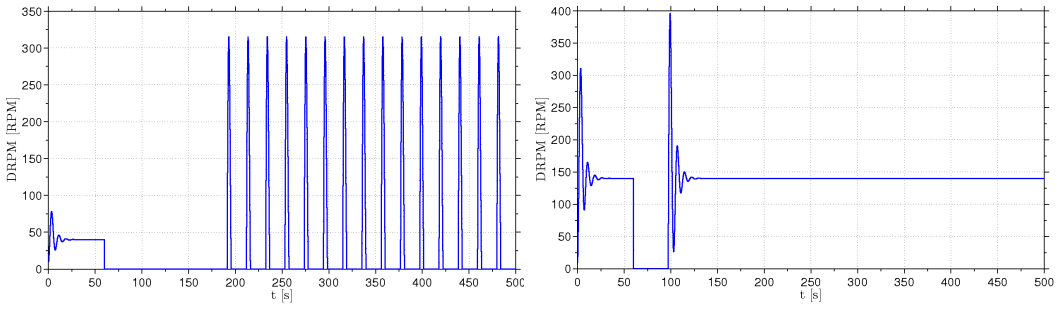

(a) (b)

Figure 3.8: Set-points of (a) 40 RPM and 100kN on vibration and (b) 140 RPM and 100 kN without vibrations.

Another stick-slip severity view is presented, i.e., how severe the stick-slip is from the different friction models. In Table 3.3 the maximum Downhole RPM (DRPM), the stick-slip severity (SSS) and the period T of each friction model (keeping the same set-point of WOBxRPM) is shown. As it is noticed in Figure 3.7, Model 6 presents the smallest net area and, according to Table 3.3, also presents the

highest amplitude of vibration for the same WOBxRPM pair [110 kN 60 RPM]. Thus, the SSS is greater. Model 6 possesses a larger transition zone between the static and dynamic friction which provides a trapping zone of vibrations. That transition zone is responsible for the trapping of the system in the stick-slip motion. Also, as expected, the period T remains almost unchanged since the drilling system proprieties (J_{BHA}, C, and K) are held constant and the set-point WOBxRPM is not changed.

Friction Models	**Max DRPM [RPM]**	**SSS [%]**	**Period T [s]**
Model 2	311.86	259.89	14.7
Model 3	312.47	260.39	14.5
Model 4	312.93	260.76	14.5
Model 6	321.12	267.59	14.8

Table 3.3: Response of the drilling system under the friction models adopted.

So far, the static friction peak is 1.1 and the dynamic friction is 1. To verify the influence of the static peak on the torsional vibration map, Model 2 with three different static friction peaks described in Table 3.4 is used. The dynamic friction value remains 1.

Different Peaks	**Friction static value**
Static Peak 1	1.1
Static Peak 2	1.3
Static Peak 3	1.5

Table 3.4: Friction static peaks.

Figure 3.9 illustrates the influence of the static friction peak on the torsional vibration map. The increase in static peak influences the increase of the zone with stick-slip, as expected.

In Figure 3.10 the influence of the dynamic point on the torsional vibration map using the friction values of the Model 2 is depicted. It is clear that a downward displacement of the torsional vibration map increases the vibration zone. This is because it has created a larger transition zone between static friction and dynamic friction points. However, a large difference of dynamic set points to verify the behavior illustrated in Figure 3.10 is needed. Table 3.5 contains the used values of the different dynamic points.

In 1994, Pavone and Desplans [29] developed a friction model from field data of the so-called Télévigile measurement device. The Télévigile was placed just above the bit and its function is to measure and to transmit data about BHA dynamics [29]. Due the experimental origin of this model, Pavone friction model is chosen as the friction model of the torque on bit in this work and is implemented using "look-up

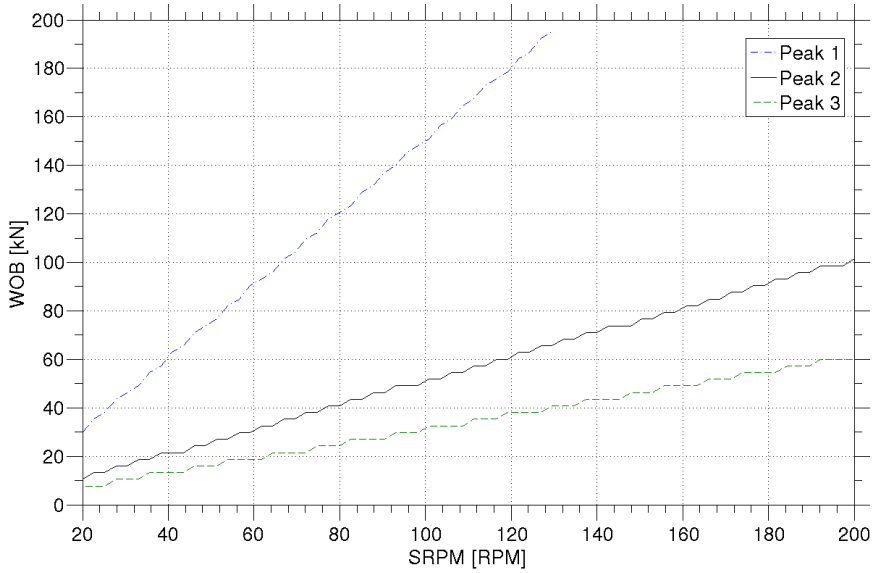

Figure 3.9: Torsional vibration map of Model 2 with different friction static peaks.

Different point	**Dyn. set point velocity [RPM]**
Space 1	3.5
Space 2	10.5
Space 3	20.5

Table 3.5: Different dynamic set points.

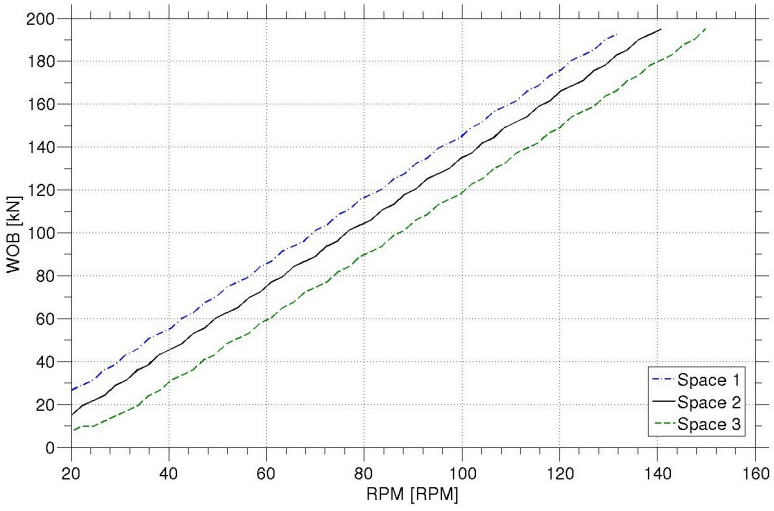

Figure 3.10: Dynamic set-point influence on the torsional vibration map.

table" function (*Simulink*). Figure 3.11 illustrates the friction model discussed. The torsional vibration map is generated and illustrated in Figure 3.12 which presents the set-points and a fitted curve.

So far, a two-dimensional (2D) analysis of the stick-slip severity (SSS) comparing different friction models at the bottom end was performed. However, the

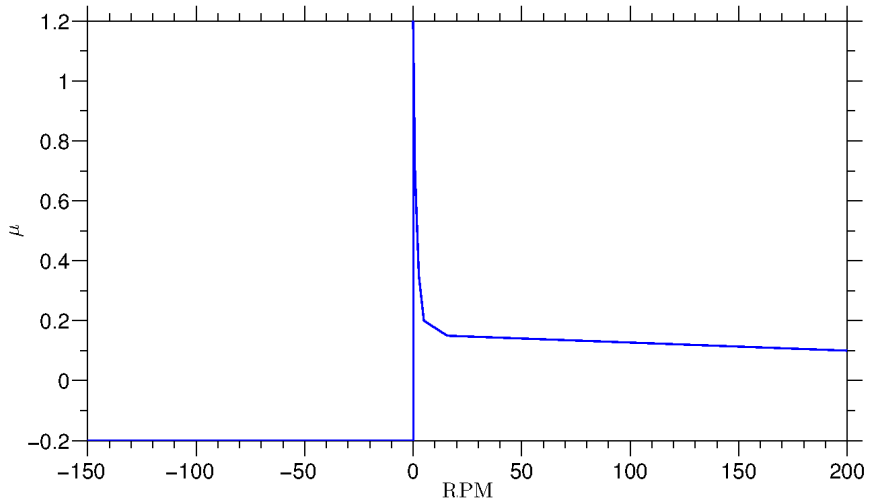

Figure 3.11: Pavone friction model.

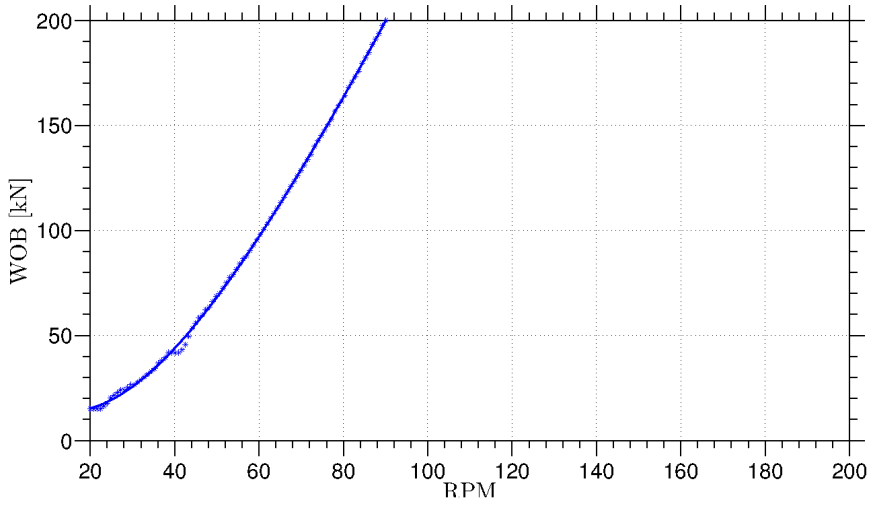

Figure 3.12: Severity curve of the system using Pavone friction model.

severity of the stick-slip must be ascertained. For this purpose, a three-dimensional (3D) SSS map with color diagram using the Pavone friction model is generated. Figure 3.13 illustrates the torsional vibration severity in the color diagram. Also, Figure 3.14 shows the level curves with the color diagram. These figures illustrate an intermediate zone which holds intermediate severity oscillations. The behavior will explain some results over this dissertation.

Using this friction model, a sensitive analysis of the parameters of the drilling system is studied with a two DOF system. The length of DP and BHA are changed and their influences are analyzed. In this analysis when the L_{DP} is changed the stiffness of the drilling system is directly influenced and the L_{BHA} influences on the moment of inertia of the bit. Figures 3.3 and 3.3 depict the behavior of the system when the length of DP and the BHA are varied. Tables 3.6 and 3.7 show the influence the L_{DP} on the stiffness and the L_{BHA} on the moment of inertia of the drilling system, respectively.

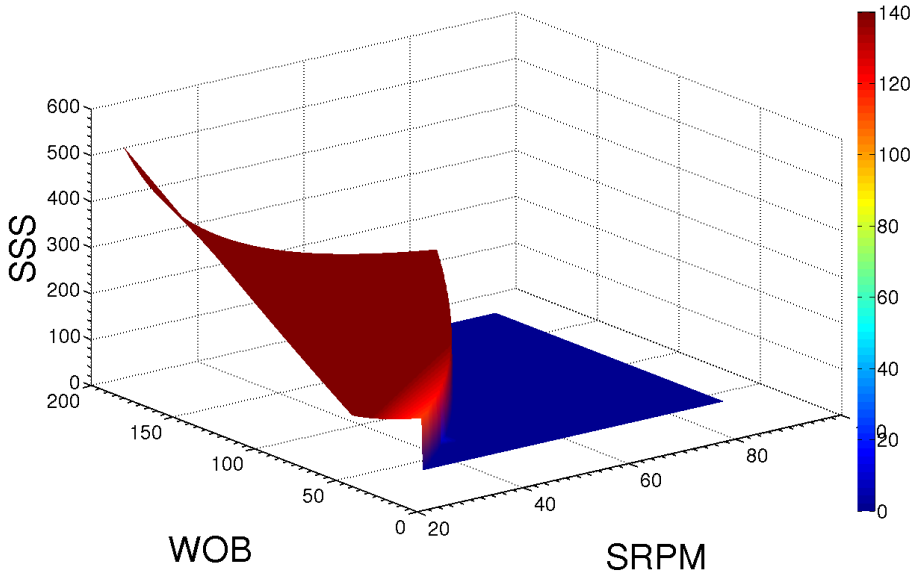

Figure 3.13: 3D stick-slip severity map.

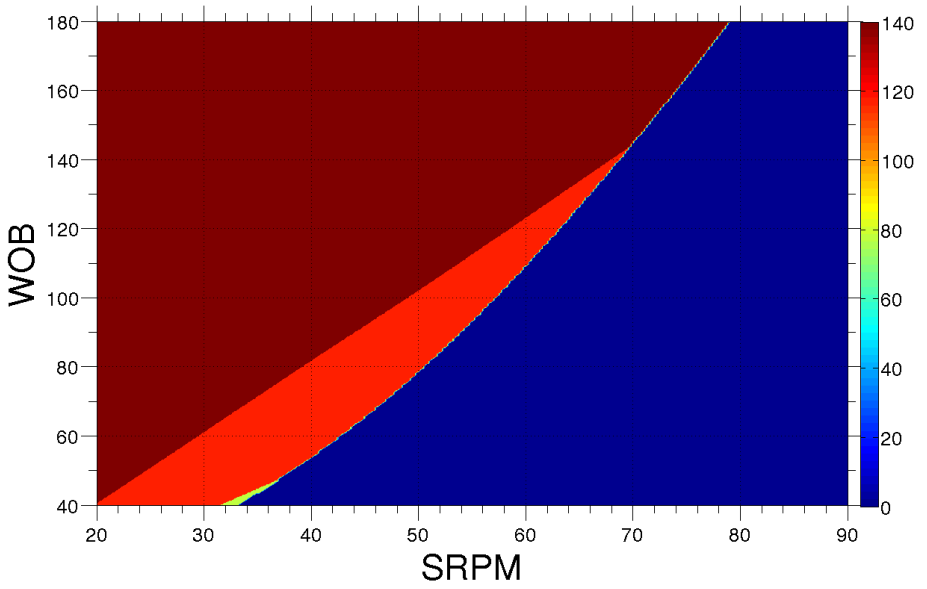

Figure 3.14: 2D stick-slip severity map.

Both graphics of Figure 3.15 illustrate a behavior of the system under the influence of lengths of drill pipes and BHA. The vibration zone increases as length of drill pipe increases because it becomes more flexible. By contrast, the increase in the length of the BHA indicates an increase of the moment of inertia, providing a greater resistance to movement and reducing vibration zone.

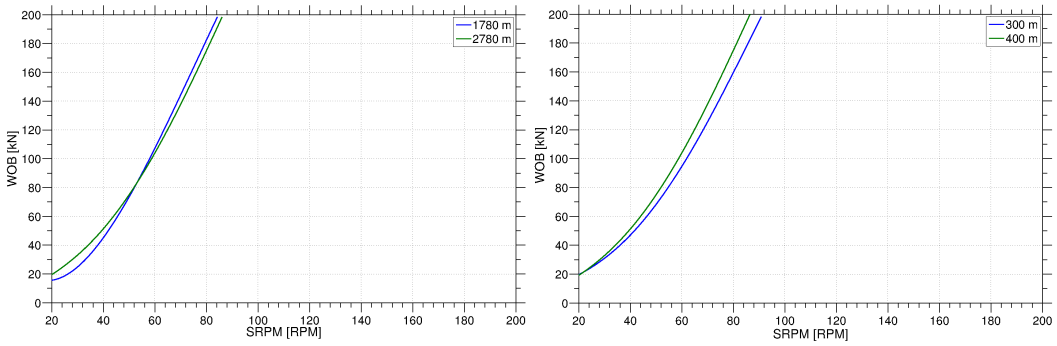

(a) (b)

Figure 3.15: Influence of the length of (a) drill pipe and (b) BHA on torsional vibration map.

Length [m]	**Stiffness [Nm/rd]**
1780	853.607
2780	546.554

Table 3.6: Length of drill pipe and stiffness values with constant BHA length (400 m).

Length [m]	**Moment of Inertia [kgm^2]**
300	439.801
400	586.402

Table 3.7: Length of bottom hole assembly (BHA) and moment of inertia values with constant drill pipe length (2780 m).

3.4 Convergence test

The study of a simple system, such as two degrees of freedom (DOF's), is important to observe phenomena and to become familiar with the system in question. Nonetheless, a better discretization is necessary to produce a proper description of the behavior of the drill string system. Therefore, in this section a convergence test is performed. For this, the dynamical torsional model of lumped parameters is discretized, increasing the number of degrees of freedom. Then, the second and third natural frequencies are observed. As assumed in section 3.2, the BHA is not discretized.

Figure 3.16 shows the convergence test to the second and the third natural frequencies. In order to choose the proper number of degrees of freedom, Figure 3.17 illustrates the relative error. With these graphs, 15 DOF's were chosen for the next simulations with the relative error of 0.054 and 0.271 %, respectively. The error is calculated according to Eq. 3-14.

$$Error = \left(\frac{Freq_{DOF} - Freq_{DOF-1}}{Freq_{DOF}} \right) \cdot 100. \tag{3-14}$$

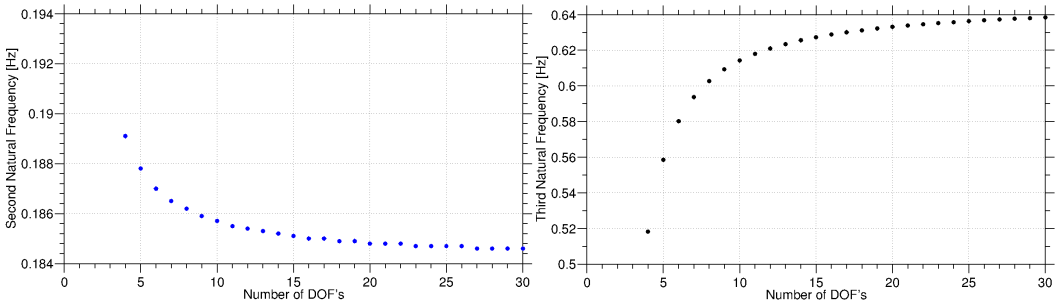

(a) (b)

Figure 3.16: Convergence test: (a) second and (b) third natural frequencies.

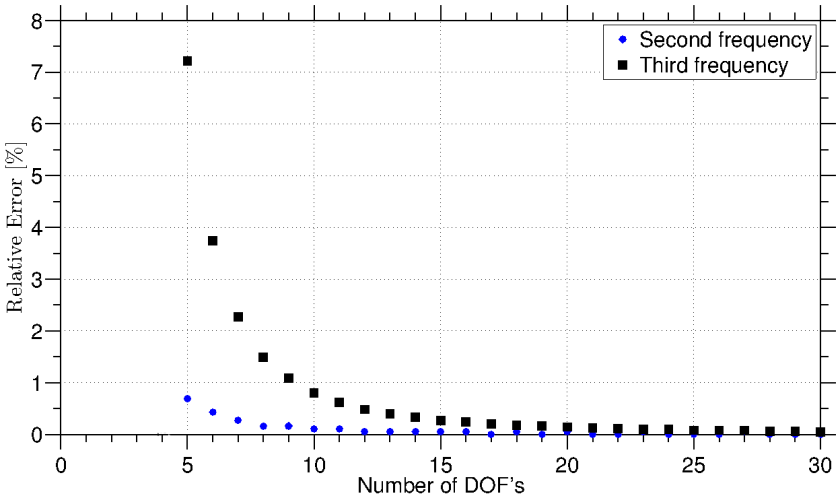

Figure 3.17: Frequencies relative error.

where $Freq_{DOF}$ is the natural frequency for the DOF in analysis, $Freq_{DOF-1}$ is the natural frequency of the previous DOF.

In this system, the first natural frequency is zero, and mode shape is a rigid body motion. It is easy to realize that the second frequency converges faster than the third. This is because higher natural frequencies and mode shapes require more degrees of freedom to be represented.

From now on, since 15 DOF's are chosen, the new torsional vibration map is necessary. For this purpose, Figure 3.18 illustrates the torsional vibration map for a 15 DOF's drilling system. It is noted that for lower RPM and WOB, the torsional vibration map presents a different shape. This is inherent to the friction model adopted because for other friction models of the section 3.3, this behavior is not noticed.

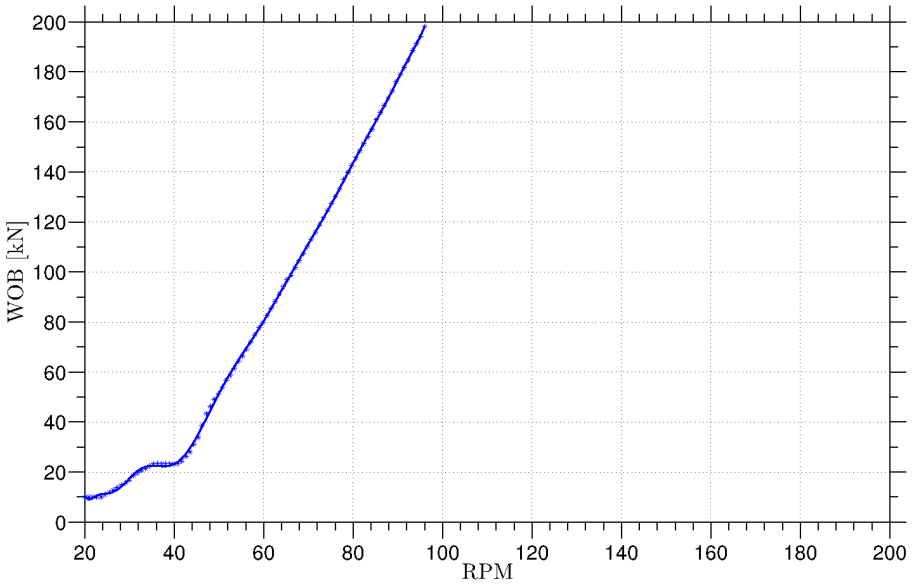

Figure 3.18: Torsional vibration map for the 15 DOF system.

3.5 Results of the full scale models

3.5.1 First model: two degrees of freedom

The bifurcation diagram is conceived with surface RPM as the control parameter for constant WOB. Also, the bifurcation diagram as a function of WOB is evaluated with constant values of SRPM. In order to construct such diagram, the maximum and minimum angular velocity of the bit is computed.

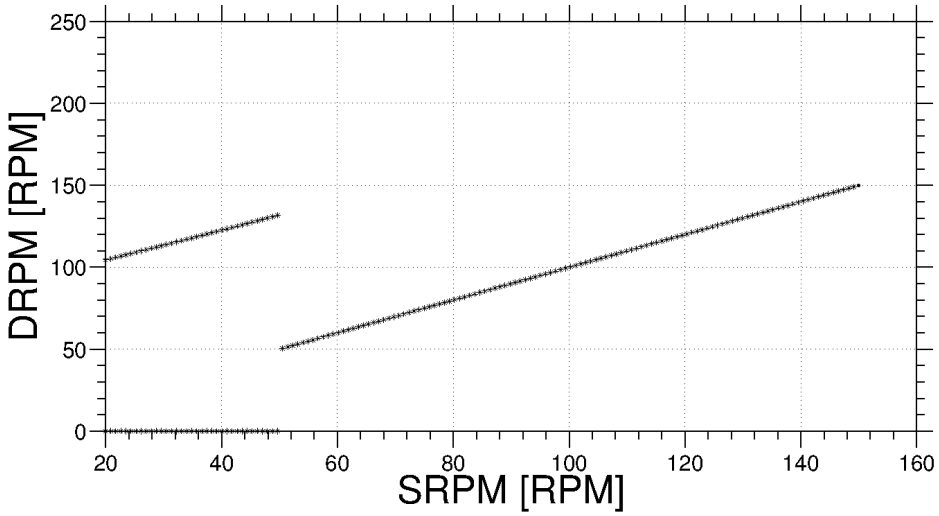

Figure 3.19: Bifurcation diagram with SRPM as control parameter and constant WOB = 80 kN.

First of all, supercritical Hopf bifurcations are observed. As expected, the amplitude of vibration increasing with different constant WOB (Figures 3.19 and

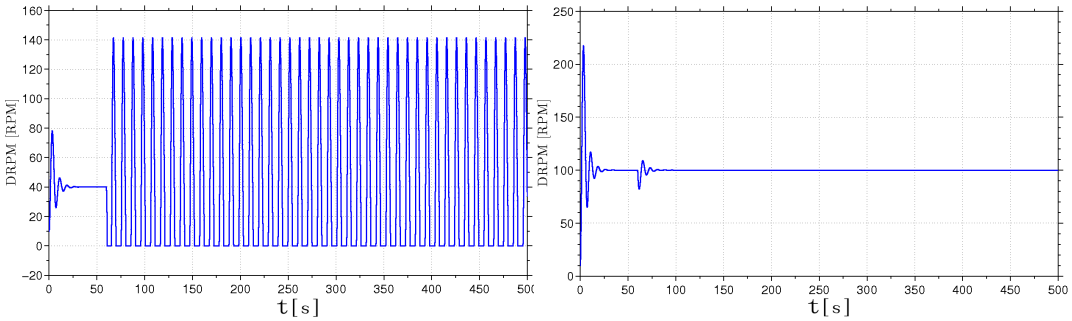

(a) (b)

Figure 3.20: Time-domain response with a constant WOB = 80 kN and (a)40 RPM and (b)100 RPM.

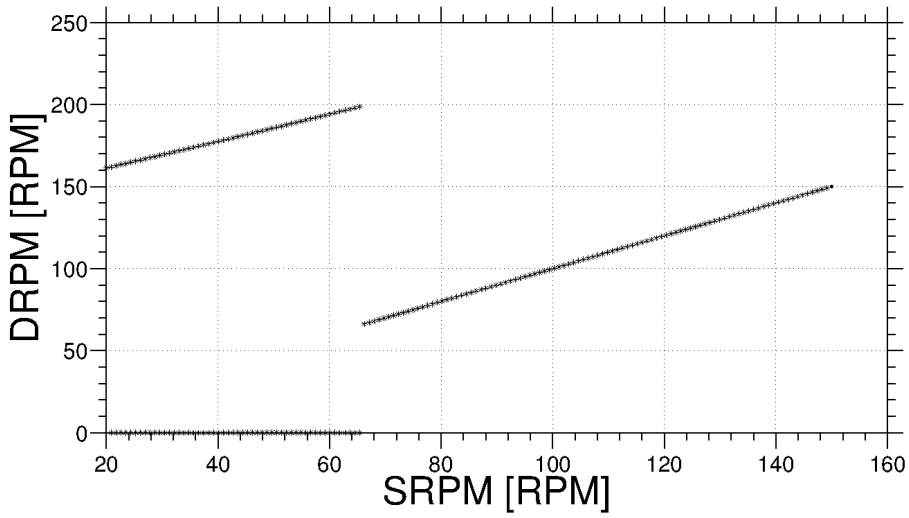

Figure 3.21: Bifurcation diagram with SRPM as control parameter and constant WOB = 130 kN.

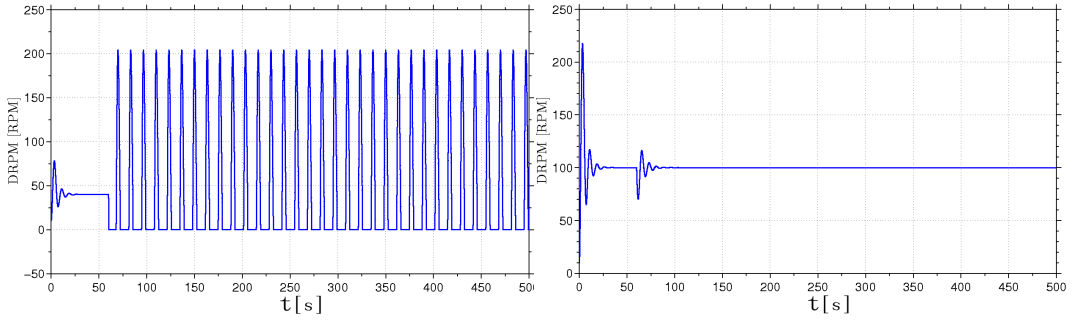

(a) (b)

Figure 3.22: Time-domain response with a constant WOB = 130 kN and (a)40 RPM and (b)100 RPM.

3.21) while the control parameter is the surface RPM at top end. Also, the bifurcation points change for different constant WOB. These figures present bifurcation points in 50.54 and 66.24 RPM, respectively, changing to new equilibrium solutions and, also, illustrate the torsional behavior of the model in a periodic solution and equilibrium point. In Figures 3.20 and 3.22 are illustrated the time-response of the torsional

behavior for a set-points of [40 RPM, 130 kN] and [100 RPM, 130 kN], respectively, depicting torsional vibrations and no torsional vibrations.

Furthermore, the vibration amplitudes for WOB as control parameter increases while the SRPM stay constant. As expected, the severity of the vibrations increases when the WOB is increased (Figure 3.23 and 3.25), and present bifurcation points in 53.83 and 184.1 kN, respectively, creating periodic solutions. The effect on the bifurcation diagram with WOB as control parameter is more visible. Figure 3.24 present the torsional behavior when it is in equilibrium point and periodic solution, respectively, as well as Figure 3.26. The difference is the set of SRPM.

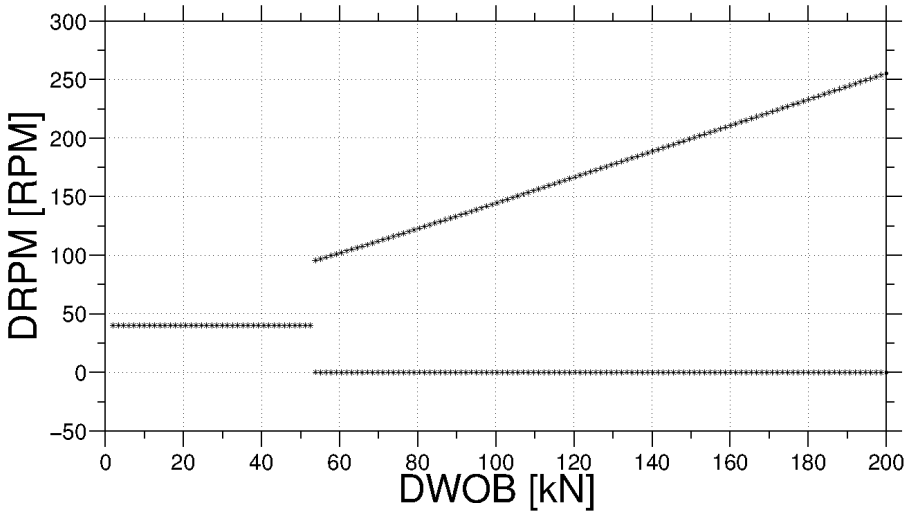

Figure 3.23: Bifurcation diagram with WOB as control parameter and constant SRPM = 40 RPM.

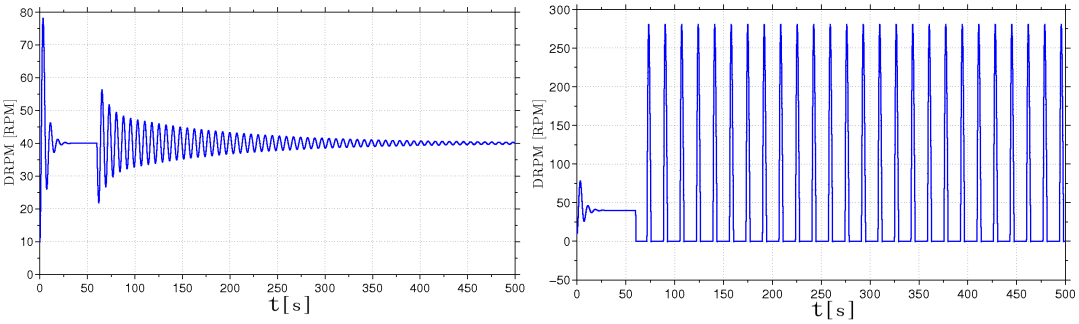

(a) (b)

Figure 3.24: Time-response with a constant SRPM = 40 RPM and (a)40 kN and (b)190 kN.

These system behaviors illustrate bifurcations between an attractor of dimension one (limit cycle) and an attractor of dimension zero (fixed point), Figures 3.19 and 3.21, and vice-versa, Figures 3.23 and 3.25, representing an asymptotic behavior [35].

A limit cycle is stable (or attracting) if the neighboring trajectories approach the limit cycle [37]. In Figure 3.27 are depicted the stable limit cycle of dimension zero

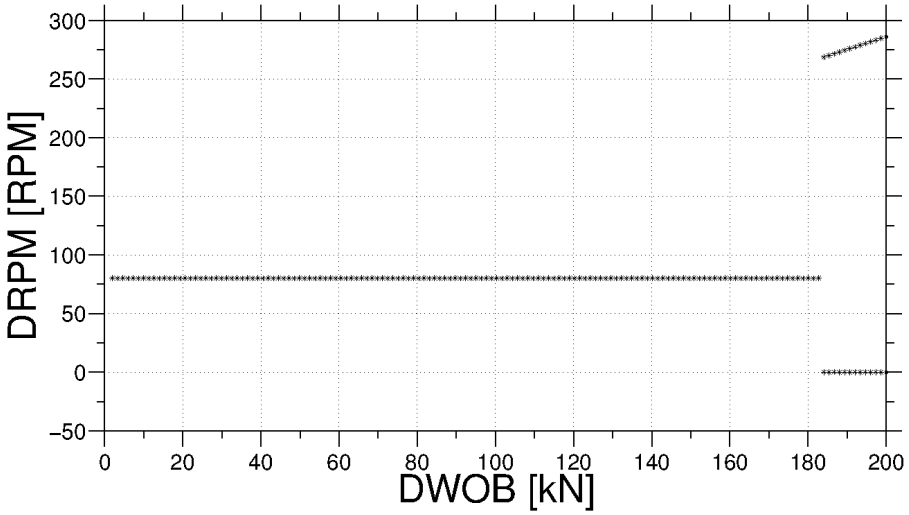

Figure 3.25: Bifurcation diagram with WOB as control parameter and constant SRPM = 80 RPM.

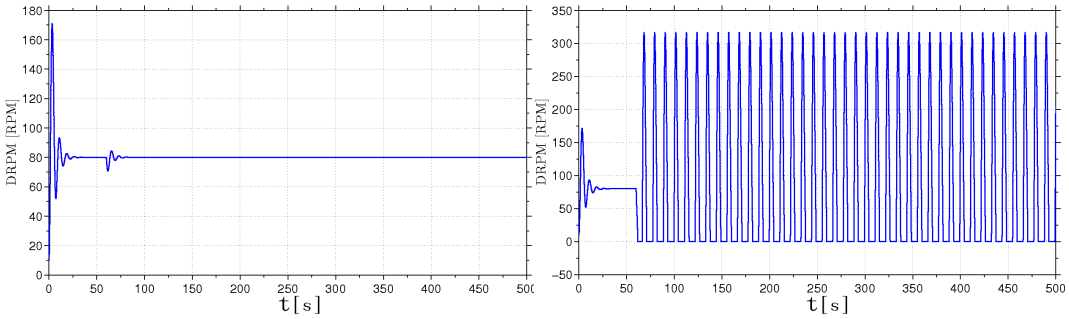

(a) (b)

Figure 3.26: Time-response with a constant SRPM = 80 RPM and (a)40 kN and (b)190 kN.

and one, respectively, with initial conditions (Eqs. 3-9) $\varphi_0 = [0\ 0]^T$ and $\Omega_0 = [0\ 0]^T$. The red lines denote the transient part of the solution.

Therefore, in order to observe the stability of the solutions above, Figure 3.28 depicts the other initial conditions $\varphi(0) = [0\ -100]^T\ rad$ and $\Omega(0) = [100\ 0]^T\ rad/s$, converging to the same limit cycles (dimension zero and one). It is noted, once again, that the equilibrium solution would have the same angular difference $(\varphi_1 - \varphi_2) = -8.353\ rad$ but after applying the resistive torque the angular difference increases $(\varphi_1 - \varphi_2) = -12.4\ rad$. Both solutions are stable.

Moreover, the Poincaré map is shown is this section. The Poincaré map enables to discuss the stability of periodic solutions or equilibrium in terms of the properties for the fixed points [13]. Analysis using Poincaré maps transforms the study of continuous time systems to the study of discrete time systems, providing a dimensional reduction [40], as explained earlier in Section 2.2.

Figure 3.31 depicts the Poincaré map with constant WOB and different SRPM. It is noticed that, for 40, 50, and 60 RPM with 110 kN, the system keep a periodic solution and for 70 RPM the closed orbit loses stability and became an equilibrium

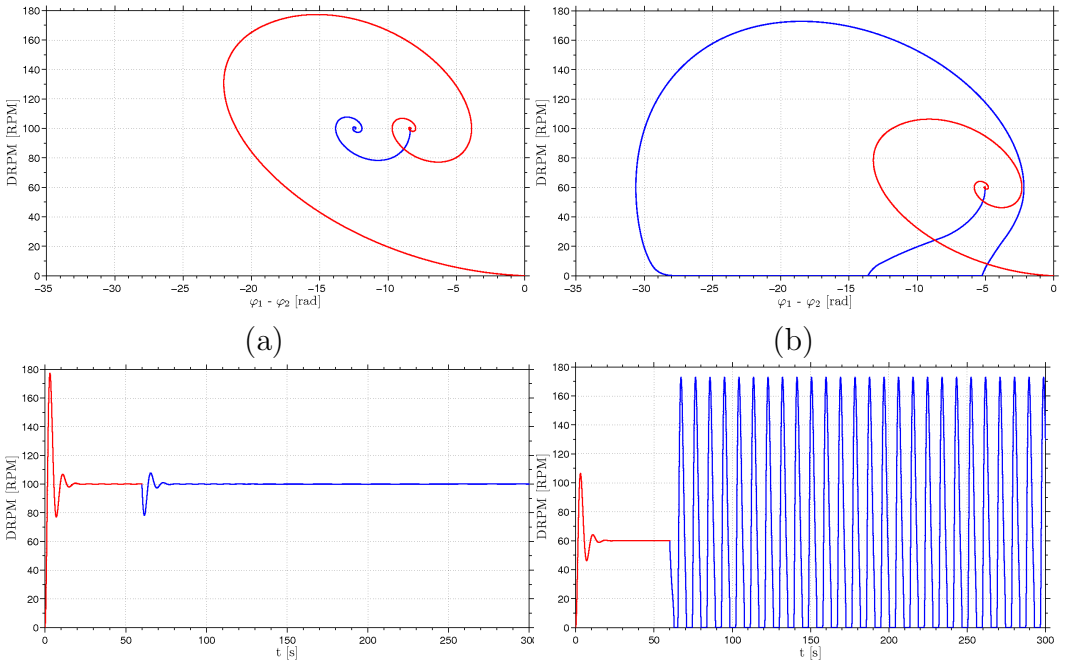

Figure 3.27: Limit cycle of dimension (a)zero and (b)one with initial conditions of 0 rad and 0 rad/s, and (c) and (d) are the time-response of the system. Set-point for (a) and (c) is $WOB = 110$ kN and $SRPM = 100$ RPM, and for (b) and (d) is $WOB = 110$ kN and $SRPM = 60$ RPM.

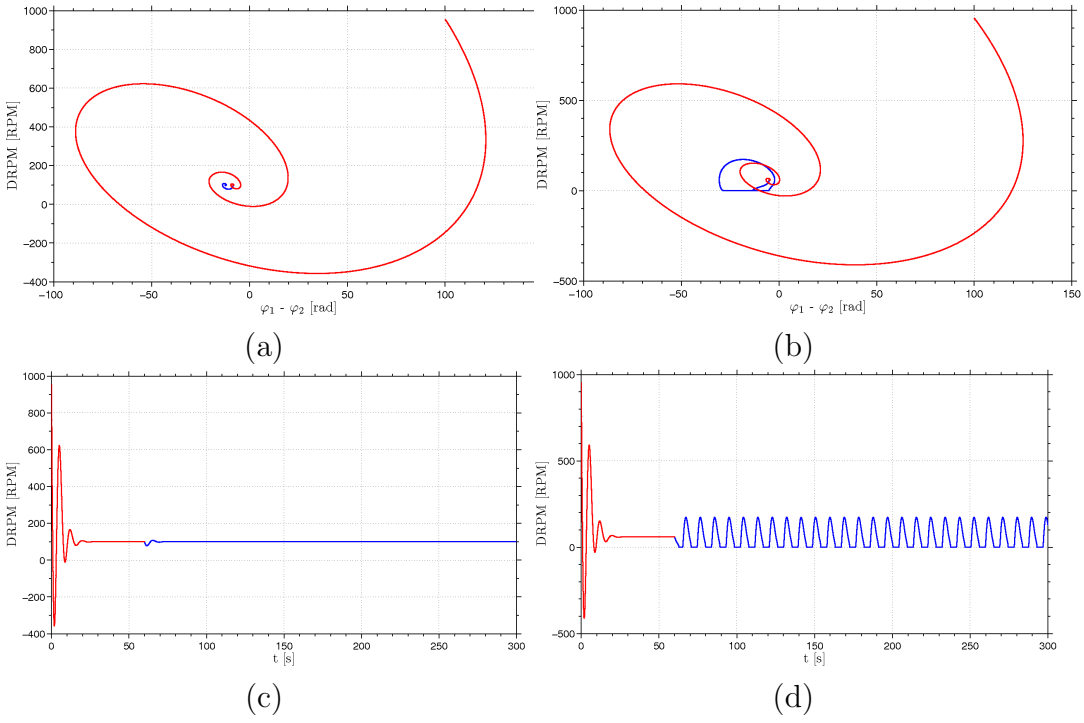

Figure 3.28: Limit cycle of dimension (a)zero and (b)one with initial conditions at surface of 100 rad and 100 rad/s, and (c) and (d) are the time-response of the system. Set-point for((a) and (c) is $WOB = 110$ kN and $SRPM = 100$ RPM, and for (b) and (d) is $WOB = 110$ kN and $SRPM = 60$ RPM.

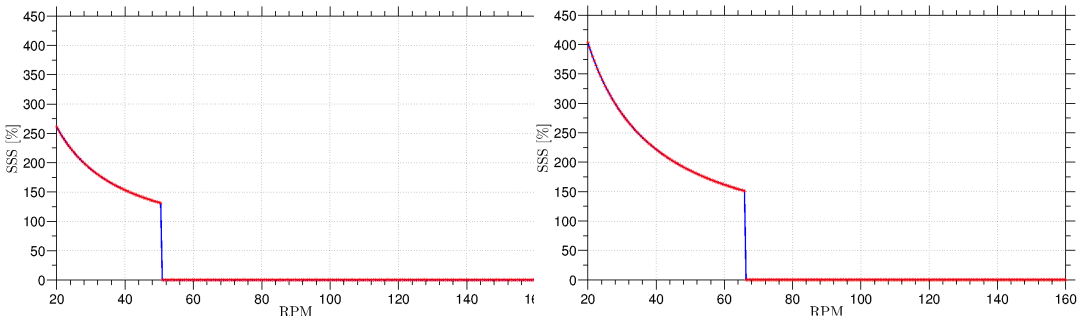

Figure 3.29: Nonlinear jump in function of SRPM with (a)WOB = 80 kN and (b)130 kN.

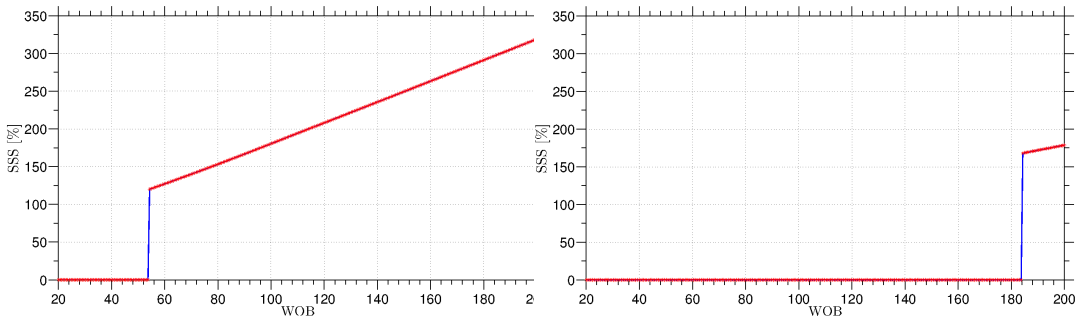

Figure 3.30: Nonlinear jump in function of WOB with (a)SRPM = 40 RPM and (b)80 RPM.

point. Figure 3.32 depicts the limit cycles of the RPMxWOB set-points of Figure 3.31.

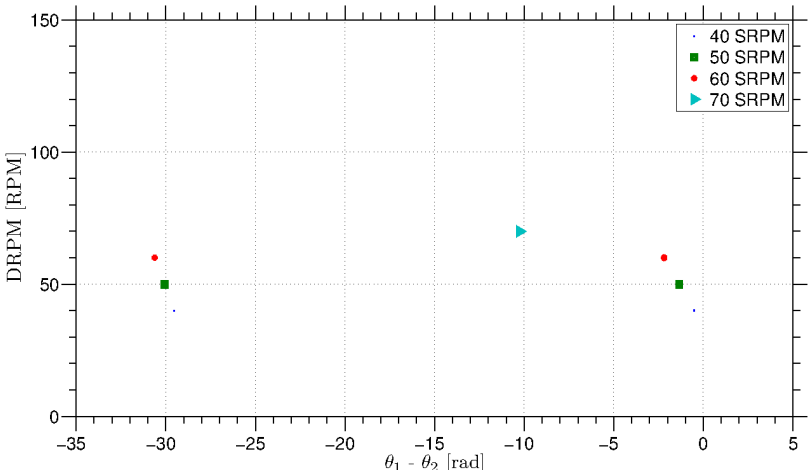

Figure 3.31: Poincaré map with $WOB = 110$ kN and different SRPM.

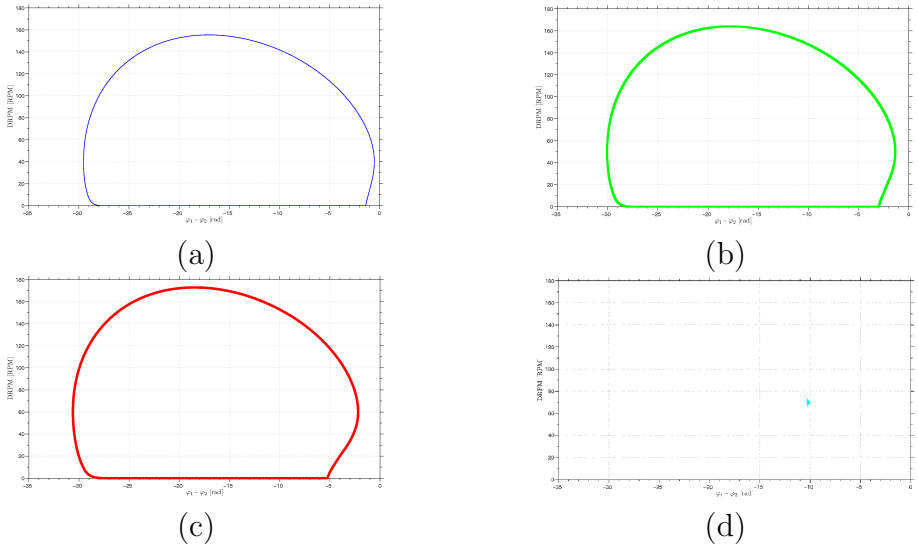

Figure 3.32: Phase plane of the different SRPM and 100 kN. (a)40 RPM, (b)50 RPM, (c)60 RPM, and (d)70 RPM.

3.5.2 Second model: multi degrees of freedom

Next, the analysis of multi degrees of freedom system is performed. As previously stated, fifteen degrees of freedom were chosen based in a convergence test (section 3.4). The bifurcation diagrams are performed, such as in the previous analysis.

Herein, supercritical Hopf bifurcations are assessed once more. Again, it is noticed the bifurcation points of the torsional dynamics of the system and they are kept with the points where there exist the nonlinear jumps. The stable solutions noted in the previous section are proven in the analysis of the limit cycles.

However, the vibration amplitudes are larger than the two DOF's modeling. Figure 3.33 depicts the creation of an equilibrium branch while increasing RPM at top end. Comparing with Figures 3.19 and 3.21, Figure 3.33(a) illustrates that the system presents no vibrations in 61.01 RPM, and reaches 187 of maximum DRPM and negative values -4.33 of DRPM. The bifurcation points are 61.01 and 77.58 RPM for 80 and 130 kN, respectively. Figure 3.33(b) shows maximum DRPM of 280 and, also, negative values -13.35 of minimum DRPM.

Likewise, in Figure 3.34 there is the behavior of the system where SRPM is kept constant while DWOB is varied. The critical state is observed: large vibration amplitudes (336 and 379 RPM), reaching negative RPM at downhole position (-15.29 and -3.03 RPM), are shown in Figure 3.34(a) and 3.34(b). Once more, the DWOB effect on the bifurcation diagram is more visible.

Figure 3.34(a) presents a intermediate vibration zone, as Figure 3.14 illustrated in section 3.3. It means that there exists a torsional vibration zone which presents lowest amplitudes, as shown in Figure 3.35. It presents a transition between the equilibrium point and the periodic solution is observed. Firstly, the periodic branch is created, reaching DRPM values close to the former equilibrium point. Afterwards,

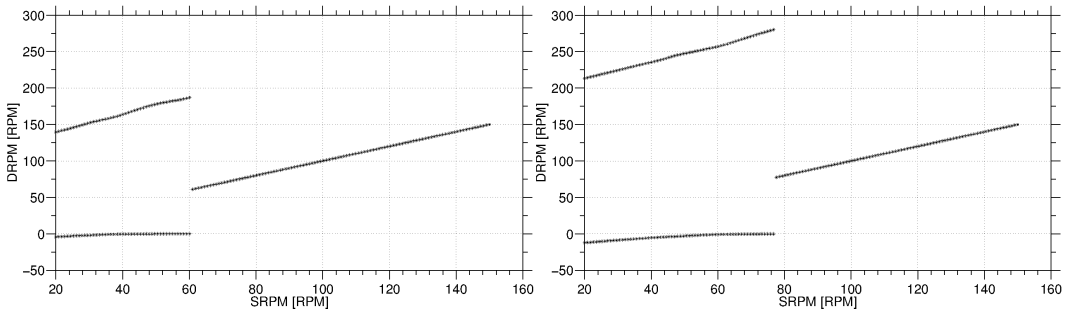

(a) (b)

Figure 3.33: Bifurcation with (a) WOB = 80 kN and (b) WOB = 130 kN.

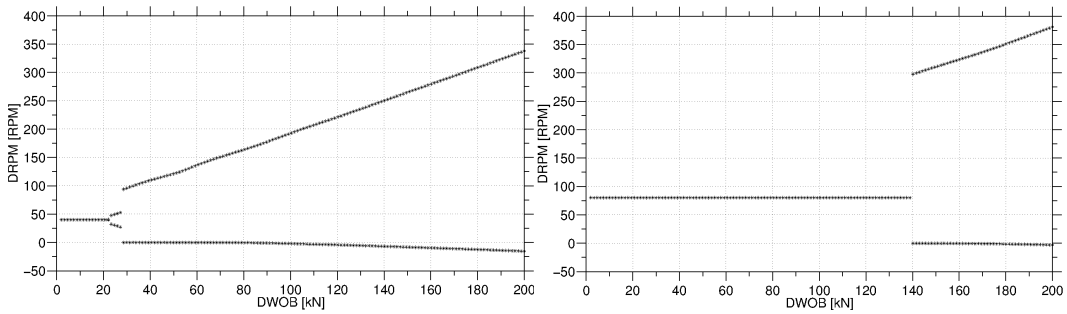

(a) (b)

Figure 3.34: Bifurcation with (a) SRPM = 40 RPM and (b) SRPM = 80 RPM.

an other bifurcation point appears and the maximum and minimum values of DRPM are larger and distant from the equilibrium branch.

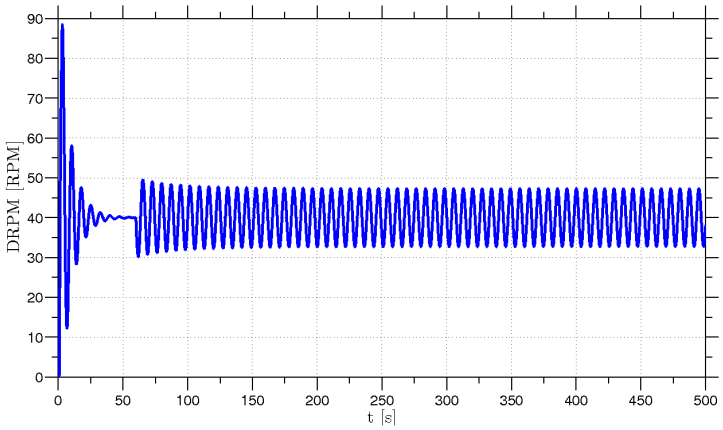

Figure 3.35: Intermediate vibration amplitudes.

As observed in section 3.5.1, the drilling system does not present unstable behavior. There exists an alternation between an attractor of one (limit cycle) and zero dimensions (fixed point). In Figures 3.36(a) and 3.36(b) there are depicted these stable limit cycle, respectively. The angular displacement relation is between the bottom and top ends $\varphi_1 - \varphi_{15}$. The time-domain responses are illustrated in Figures 3.36(c) and 3.36(d).

In order to exemplify the attraction of these solutions, the initial conditions are changed. $\varphi_1(0) = 0$ and $\varphi_{15}(0) = -100$ rad, and $\Omega_1(0) = 100$, $\Omega_{15}(0) = 0$ rad/s are chosen, as previous section, in order to observe the stability of these solutions. The other DOF's initial conditions are zero. Figure 3.37(a) 3.37(b) illustrate how far from the stable point (or orbit) are these initial conditions. Also, the time-domain responses are depicted in Figures 3.37(c) and 3.37(d).

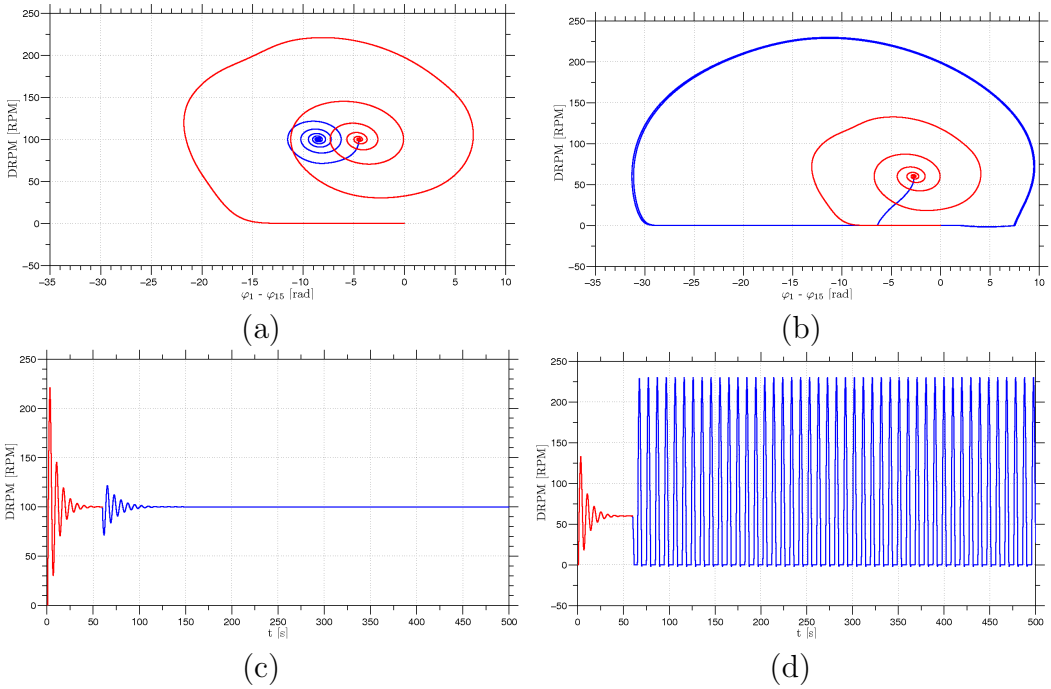

Figure 3.36: Limit cycle of (a) zero (WOB = 110 kN and SRPM = 100 RPM) and (b) one dimension (WOB = 110 kN and SRPM = 60 RPM) with initial conditions of 0 rad and 0 rad/s. (c) and (d) are the time-domain response of (a) and (b), respectively.

The nonlinear jumps of the *SSS* for the fifteen DOF's model are performed and depicted in Figures 3.38 and 3.39. As noted in previous section, these nonlinear jumps occur exactly at the bifurcation points where the current solution jumps to another equilibrium solution (Figure 3.33) or a periodic solution (Figure 3.34).

An intermediate *SSS* zone is created and afterwards an other bifurcation occurs.

3.6 Conclusion

In this chapter, the mathematical model was presented. The equations of motion for two and multi degrees of freedom was approached in order to construct the matrices of properties of the drilling system.

Also, the sensitivity analysis of the friction models was performed. These analysis illustrated the behavior of the system under different resistive torques, simulating the interaction bit-rock. Four friction models were created and applied on

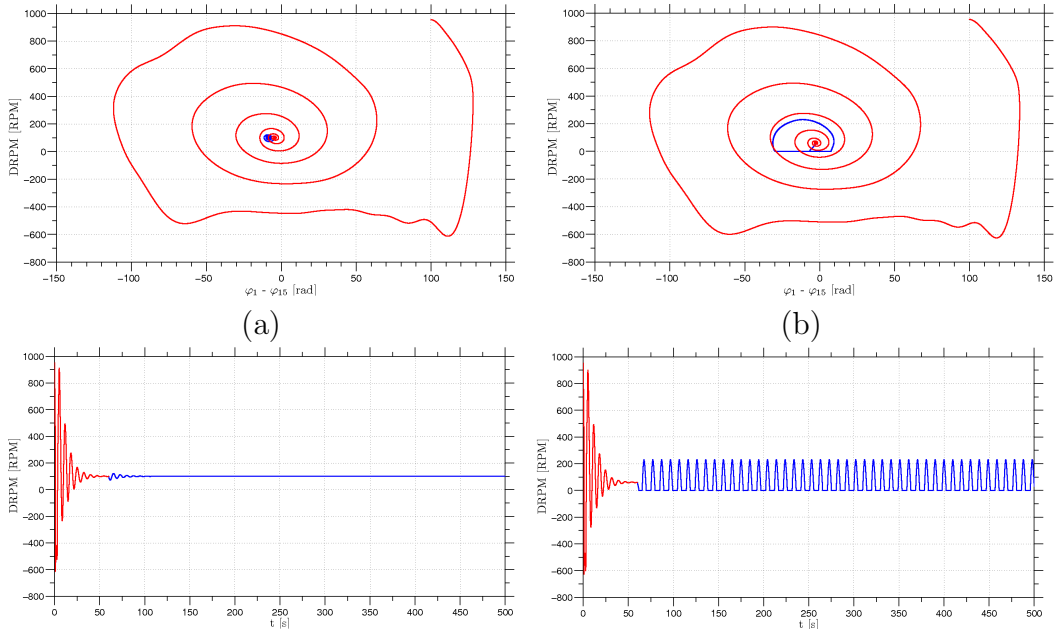

Figure 3.37: Limit cycle of (a) zero (WOB = 110 kN and SRPM = 100 RPM) and (b) one dimension (WOB = 110 kN and SRPM = 60 RPM) with initial conditions of 100 rad and 100 rad/s. (c) and (d) are the time response of (a) and (b), respectively.

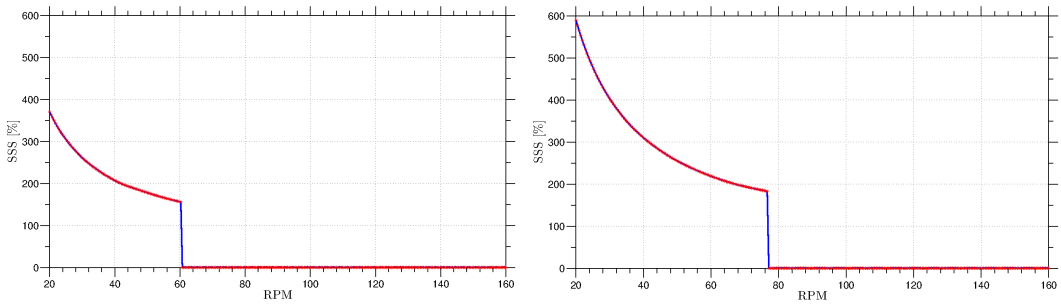

Figure 3.38: Nonlinear jump as function of SRPM with (a) WOB = 80 kN and (b) WOB = 130 kN.

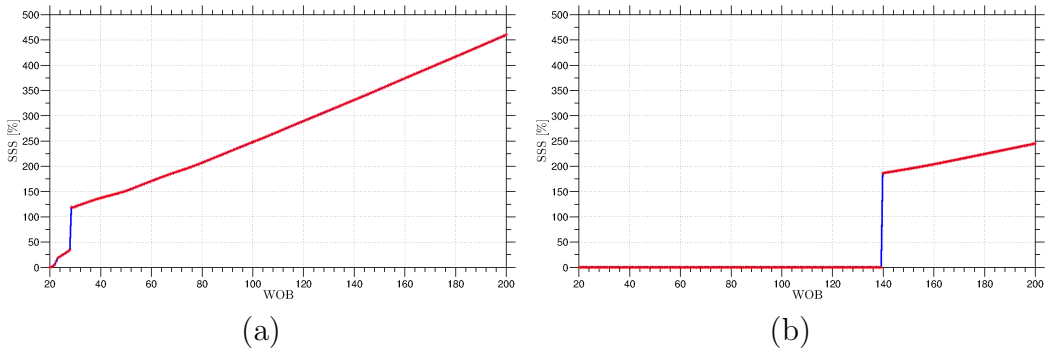

Figure 3.39: Nonlinear jump as function of WOB with (a) SRPM = 40 RPM and (b) SRPM = 80 RPM.

the system. The torsional vibration maps, which distinguish zones with and without vibrations, are discussed and compared. The chosen friction model was Pavone friction which presented field data, extracted from [29]. Once again, the behavior of the system was observed under Pavone friction. A convergence test to identify the proper number of degrees of freedom (NDOF) was concluded. The second and third natural frequencies were compared in each discretization. Figures depicted the evolution of these frequencies in function of NDOF, as well as the relative error in function of NDOF. Fifteen degrees of freedom were enough to the model convergences with acceptable relative errors.

The nonlinear behavior of the models was discussed. Both models, two and fifteen degrees of freedom, presented similar qualitatively behavior under same conditions of $SRPM$ and WOB. Bifurcation points and nonlinear jumps have changed, however the stability of the equilibrium point (or periodic solution) has not changed, i.e the system continued presenting two stable solutions.

Therewith, the nonlinear jumps of the SSS provide an important visual tool to avoid (or eliminate) torsional vibrations. The Hopf bifurcation diagrams offer how severe (or not) are the torsional vibrations in terms of amplitudes at bottom end and, if they are acceptable or not in operation. For instance, since the system does not present torsional vibrations and it is necessary to change the set-points of [$SRPM$,WOB], check these graphics may prevent undesired motions. Now, suppose a drilling system presenting torsional vibrations and the mitigation (or elimination) of them is required, then the next set-points may be visualized in Figures 3.19, 3.21, 3.23, and 3.25 and a best choice can be taken. In general words, the relative fast computational acquirement (comparing with finite element models, for example) of these results provides tools for a best and fast decision about torsional vibration problems in field.

However, the nonlinear jump showed that the behavior persists if the RPM (or WOB) starts from zero (blue line) or from 160 RPM (red stars). It means that the torsional system holds only one attractor into each zone (with or without vibration) and does not identify the difference of increasing or decreasing of RPM (or WOB), typically encountered in nonlinearities. Thereby, the simulations showed that the system owns two stable solutions: vibration and no vibration. Nevertheless, there existed only one attractor depending of the zone which the point was.

The axial dynamics is intrinsically linked to the torsional dynamics of the drilling system [30]. Then, the results of such coupling motions may provide different graphs about nonlinear jumps of SSS and bifurcation points and diagrams.